

Solution-Synthesized Chevron Graphene Nanoribbons Exfoliated onto H:Si(100)

Adrian Radocea,^{†,‡} Tao Sun,^{†,§} Timothy H. Vo,[⊥] Alexander Sinitskii,^{⊥,#} Narayana R. Aluru,^{†,§} and Joseph W. Lyding^{*,†,||}

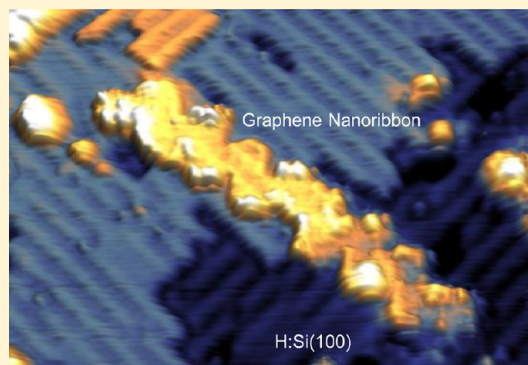
[†]Beckman Institute for Advanced Science and Technology, [‡]Department of Materials Science and Engineering, [§]Department of Mechanical Science and Engineering, and ^{||}Department of Electrical and Computer Engineering, University of Illinois at Urbana—Champaign, Urbana, Illinois 61801, United States

[⊥]Department of Chemistry and [#]Nebraska Center for Materials and Nanoscience, University of Nebraska—Lincoln, Lincoln, Nebraska 68588, United States

S Supporting Information

ABSTRACT: There has been tremendous progress in designing and synthesizing graphene nanoribbons (GNRs). The ability to control the width, edge structure, and dopant level with atomic precision has created a large class of accessible electronic landscapes for use in logic applications. One of the major limitations preventing the realization of GNR devices is the difficulty of transferring GNRs onto nonmetallic substrates. In this work, we developed a new approach for clean deposition of solution-synthesized atomically precise chevron GNRs onto H:Si(100) under ultrahigh vacuum. A clean transfer allowed ultrahigh-vacuum scanning tunneling microscopy (STM) to provide high-resolution imaging and spectroscopy and reveal details of the electronic structure of chevron nanoribbons that have not been previously reported. We also demonstrate STM nanomanipulation of GNRs, characterization of multilayer GNR cross-junctions, and STM nanolithography for local depassivation of H:Si(100), which allowed us to probe GNR–Si interactions and revealed a semiconducting-to-metallic transition. The results of STM measurements were shown to be in good agreement with first-principles computational modeling.

KEYWORDS: graphene nanoribbons, armchair edges, scanning tunneling spectroscopy, current imaging tunneling spectroscopy, silicon, dry contact transfer



Cai et al. first demonstrated the synthesis of atomically precise GNRs via the on-surface Ullmann coupling of halogenated aromatic precursors into 7-AGNRs—armchair GNRs that are seven carbon atoms wide.¹ The GNR bandgap and its electronic properties can be tuned by changing the starting precursor, and 13-AGNRs,² 15-AGNRs,³ and $N = 6$ zigzag edge GNRs⁴ have been synthesized. Unique nanoribbon geometries such as chevrons and nanoribbon heterojunctions have also been explored.^{1,5–7} Nitrogen^{8,9} and boron¹⁰ can be incorporated into the starting precursors to further modify the GNR band structures. The versatility of bottom-up synthesis promises sophisticated GNR electronics, including transistors and quantum dot qubits,¹¹ which exhibit long spin coherence times.¹² To fabricate GNR devices, the development of a clean transfer is needed to move nanoribbons from the metal growth surface onto a device compatible substrate such as SiO₂. A wet transfer method previously demonstrated leaves organic residue that degrades device performance.¹³ Although there has been recent progress in the growth of nanoribbons directly onto semiconducting germanium substrates, those nanoribbons do not achieve control over GNR width, resulting in bandgap

variability and widths that increase with increasing GNR length.¹⁴

The scalable fabrication of GNRs via solution synthesis^{15,16} promises an avenue toward large-scale GNR manufacturing if problems associated with residue can be addressed. While edge functionalization facilitates deposition by increasing GNR solubility,^{17,18} the alkyl groups may hinder electronic transport, especially in inter-GNR nanojunctions. So far, detailed electronic characterization has been limited for solution-synthesized nanoribbons, in part due to the use of ambient solvent-based deposition processes that interfere with STM spectroscopic characterization. In this study, we avoid problems with residue while depositing armchair edged chevron GNRs directly onto H:Si(100) using a dry contact transfer (DCT) procedure previously developed to study carbon nanotubes¹⁹ and graphene nanoflakes.²⁰ STM spectroscopy of this clean system reveals a 2.85 eV GNR bandgap, localized electronic

Received: September 3, 2016

Revised: December 5, 2016

Published: December 6, 2016

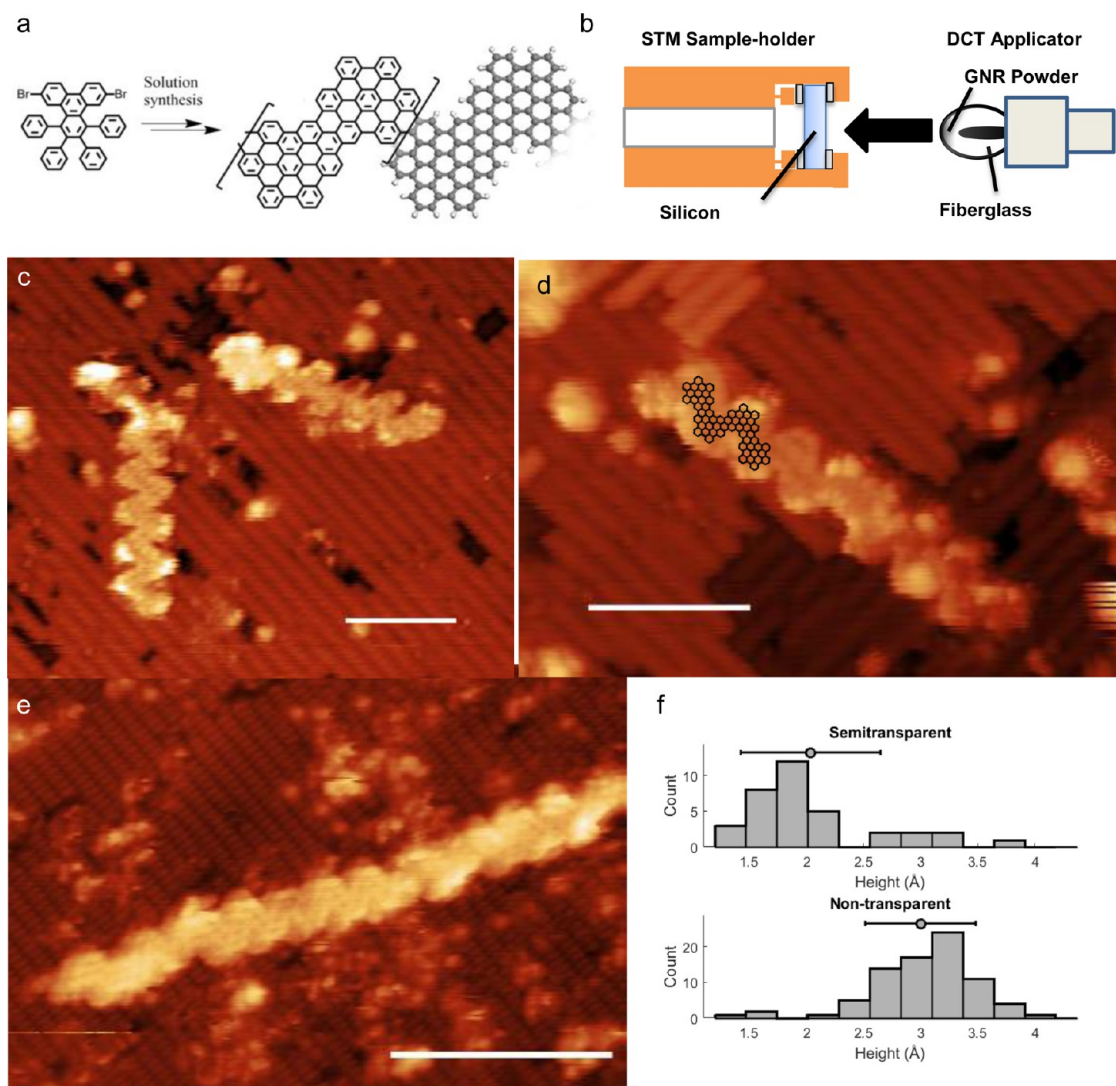


Figure 1. Scanning tunneling microscopy (STM) images of graphene nanoribbons (GNRs) on H:Si(100). Sample bias: -2 V; tunneling current: 10 pA. (a) Schematic showing precursor used for solution synthesis of chevron GNRs; see ref 15 for the detailed synthetic procedure. (b) Sketch of dry contact transfer method used to exfoliate GNRs onto H:Si(100) (c, d) Graphene nanoribbon transparency; the silicon substrate is visible through the graphene nanoribbon. Scale bar is 5 nm. (e) Image showing intraribbon resolution corresponding to the graphene lattice. Scale bar is 5 nm. Tunneling current is 100 pA. (f) Histograms of semitransparent and nontransparent GNR heights.

states, and metallic behavior for GNRs in contact with deliberately unpassivated silicon. The high spatial resolution spectroscopy achieved shows details of the electronic structure of chevron GNRs that have not yet been previously reported. Depassivating H:Si(100) via STM nanolithography allows the study of GNR–Si interactions, showing a semiconducting-to-metallic transition. We also find bilayer GNR junctions on the surface, formed by overlapping GNRs. We compare these results to first-principles density functional theory (DFT) simulations.

Results. The solution synthesis of chevron GNRs used for this study (Figure 1a) is described in a previously published protocol.¹⁵ From the synthesis, a graphene nanoribbon powder is obtained, which is then applied to a fiberglass applicator. A high temperature degas of the GNR-coated fiberglass applicator removes solvents and atmospheric contaminants. When the DCT applicator is manually pressed against the silicon surface under ultrahigh vacuum, nanoribbons cleanly exfoliate onto the surface (Figure 1b). Figure 1c is a room temperature STM image showing two chevron GNRs lying flat on the surface.

Although the STM topographs in Figure 1 were all recorded at a sample bias of -2 V and a tunneling current of 10 pA, different imaging artifacts appear, potentially caused by variations in the density of states of the STM probe.

A high-resolution image (Figure 1e) shows intraribbon resolution not corresponding to the silicon dimer rows. The STM images presented in Figure 1 are suggestive of a clean transfer process when compared to previous STM imaging of GNRs transferred onto gold via solution deposition.¹⁵ The graphene nanoribbons do not appear to align to the silicon lattice, indicating a weak coupling interaction (Supporting Information Figure S1). In Figure 1c–e silicon rows and individual dimers appear underneath the GNRs. This semitransparency effect was previously observed for graphene flakes on III–V semiconductors and arises when the forces between the tip and the flake push the graphene closer to the surface.²¹ A similar effect was not observed for graphene flakes <8 nm in diameter on H:Si(100).²⁰ In contrast to graphene nanoflakes, the atomically precise chevron nanoribbons studied do show semitransparency, due to having a bandgap larger than the

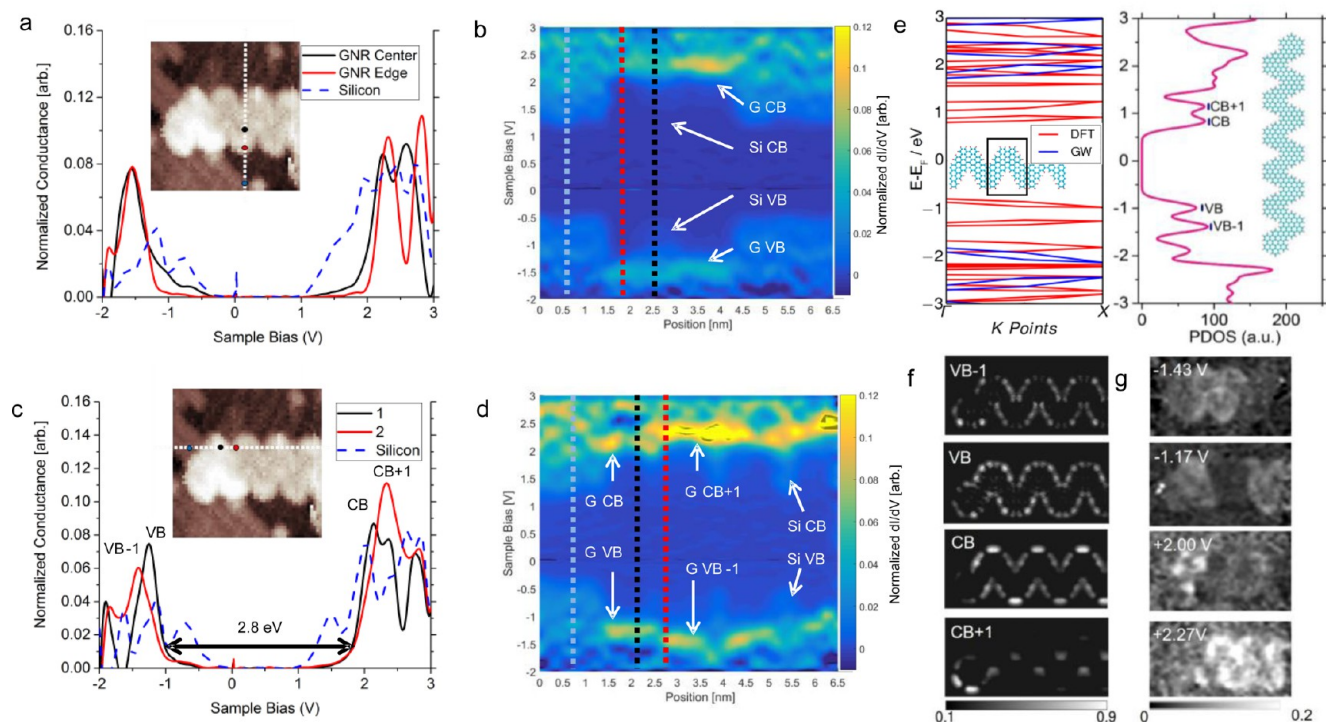


Figure 2. STS and CITS of graphene nanoribbon. Current imaging tunneling spectroscopy was collected over an array of 50×50 points spanning $6.5 \times 6.5 \text{ nm}^2$. The normalized tunneling conductance $dI/dV/(I/V)$ was numerically calculated, and portions of the data are shown here. (a) Normalized tunneling conductance at the GNR center, the GNR edge, and over the silicon substrate. The inset shows a topograph of the GNR studied. (b) Normalized tunneling conductance spectra map across the width of the GNR, corresponding to positions along the dashed white lines in the inset of (a). The black, blue, and red dashed lines indicate the positions of the spectra points shown in (a). The conduction and valence bands for the graphene and silicon are indicated. (c) Normalized dI/dV collected at two points along the edge of the GNR and the H:Si(100) substrate. (d) Normalized tunneling spectroscopy along the dashed line in (c), with lines indicating the positions of the points used to plot the data in (c). (e) Left: the band structure obtained from both DFT and GW for an infinite GNR with periodic boundary condition (the inset shows the unit cell as incorporated in the black rectangle). The band energies were shifted so that the Fermi level was located at the midgap position. Right: the projected density of states (PDOS) for an isolated six-unit cell GNR (atomic structure shown in inset, cyan atoms for C, and red atoms for H) computed using DFT. Four states VB-1, VB, CB, and CB+1 are marked at the corresponding peaks; the window is set to be 0.1 eV to be consistent with the resolution of room temperature STM experiments. (f) DFT-simulated normalized LDOS maps of the VB-1, VB, CB, and CB+1 states at 4 Å above the GNR plane; the color range of [0.1, 0.9] is used to show features more clearly. (g) Normalized dI/dV maps at energies corresponding to the bands indicated in (d).

underlying substrate, allowing the silicon density of states to dominate the tunneling current.

Of 115 GNRs imaged at both positive and negative sample bias, 80 are imaged as nontransparent, exhibiting an average apparent height of 3.0 Å relative to the surrounding silicon substrate. The 35 semitransparent nanoribbons had an average apparent height of 2.0 Å. An example of the analysis applied to determine GNR heights is shown in Figure S2. Semitransparency is not an intrinsic property of GNRs, but an imaging artifact that arises when the STM probe pushes the GNR closer to the surface, allowing the tunneling current from the substrate to contribute to the STM topograph. As shown in Figure S3, the same GNR can appear as semitransparent or nontransparent under the same sample bias and tunneling current. Semitransparency is influenced by the tip-sample separation which can vary with the work function of the STM probe as well as the interaction of the graphene nanoribbon with the surface. Chevron GNRs imaged on Au(111) show an apparent height of 1.8 Å,¹ which is significantly smaller than the apparent height observed for the nontransparent nanoribbons on H:Si(100). A previous study determined a 3.1 Å apparent height for graphene nanoflakes on H:Si(100).²⁰ The graphene lattice is only observed for nontransparent GNRs, indicating

that the carbon plane is at a height near 3.0 Å. Since the interlayer spacing of graphite is 3.3 Å, a van der Waals bonding interaction between the GNR and the H:Si(100) substrate is possible, although the apparent height indicates the local density of states (LDOS) and is not sufficient to determine atomic positions. The H:Si-GNR interaction is weak enough to enable movement of the GNR using the STM tip as shown in Figure S4.

DFT modeling of chevron GNRs, including the results shown in Figure 2e, predicts a 1.50–1.57 eV bandgap.^{15,22,23} While for graphene nanostructures DFT captures reliable information about energy level ordering, orbital shapes, and the spatial distribution of the LDOS,⁴ it underestimates bandgaps. Corrections to DFT modeling made with the GW approximation predict an expected quasi-particle bandgap of 3.62–3.74 eV.^{22,23} However, when the substrate is included in the simulation, a screening interaction further decreases the GNR bandgap.^{2,24–26} The estimated bandgap for chevron GNRs on Au(111) is predicted to be 2.96 eV.²³

UV-vis-NIR spectroscopy and photoluminescence spectroscopy of solution-synthesized nanoribbons suggest a 1.6–1.8 eV bandgap for ensembles of GNRs.^{16,27} However, these measurements probe the optical bandgap and neglect the

exciton binding energy. The quasi-particle bandgap determined with angle-resolved ultraviolet photoemission (ARUPS) studies of chevron GNRs on Au(788) is 3.1 ± 0.4 eV,²⁸ and high-resolution energy electron loss spectroscopy (HREELS) estimates a 2.8 ± 0.3 eV bandgap,⁸ in close agreement with the theoretical GW predictions. STS data for pristine chevron GNRs on Au(111) are presented in two recent studies and similar bandgaps of 2.0 eV were reported.^{6,27} Studying the bandgap of solution-synthesized GNRs on H:Si(100) is important to confirm their electronic properties and in understanding how GNR-H:Si(100) interactions modify the bandgap.

STM spectroscopy of GNRs is sometimes limited to point spectroscopy¹⁴ and tunneling conductance (dI/dV) maps^{2,6} which may not fully capture the electronic landscape of GNRs. In our work current imaging tunneling spectroscopy (CITS) was used to collect $I-V$ spectra over 50×50 points to examine a GNR and the surrounding substrate at 512 sample biases between -2 and $+3$ V. Bandgap determination of atomically thin GNRs requires careful analysis because STS simultaneously probes both the GNR and the substrate. For GNRs on Au(111), a broadened surface state prevents the observation of the edge state of atomically precise zigzag GNRs.^{4,29} In this work, the STS measurements of chevron GNRs on H:Si(100) also show a significant substrate contribution.

Figure 2a shows normalized conductance plots for three of the points collected with CITS, corresponding to the GNR center, GNR edge, and the H:Si(100) surface. Spectroscopy measured at the GNR center shows additional features resembling the peaks observed over the silicon substrate, indicating that the surface is contributing to the STS measurement (see Figure S10). Remarkably, the silicon surface electronic structure is less pronounced at the GNR edge. A normalized conductance spectra map shown in Figure 2b shows how the density of states varies along the width of the GNR. The dashed vertical lines indicate the positions of the points plotted in Figure 2a. The normalized conductance at the center of the GNR shows contributions from the silicon valence band (VB) and conduction band (CB), shifted from their original positions due to interactions with the GNR. At higher energies tunneling conductance peaks appear due to the GNR conduction and valence band states. To more clearly depict the GNR states, spectroscopy collected along the edge of the GNR is shown (Figure 2c,d).

The normalized tunneling conductance spectral traces shown in Figure 2c and the corresponding spectra map shown in Figure 2d highlight states at -1.47 , -1.17 , 2.0 , and 2.27 V, which are identified as the GNR VB-1, VB, CB, and CB+1 states. To ensure that the GNR states are identified correctly, first-principles simulations were used to simulate an infinite GNR with periodic boundary conditions and an isolated GNR comprising six unit cells (all edges terminated with hydrogen atoms) with a length comparable to that of the GNR experimentally examined. Figure 2f shows simulated normalized LDOS maps produced by selecting peaks in the DFT-calculated projected density of states (PDOS) indicated in Figure 2e and mapping them onto spatial coordinates for the six-unit-cell GNR. The LDOS contours are shown at a constant height of 4 Å above the graphene plane. We estimate the distance between the tip and graphene sample plane is 4 Å. Tip-sample separation has previously been shown to have a significant effect on dI/dV imaging because of the three-dimensional distribution of the GNR LDOS.⁷ (Additional LDOS maps at

varying heights above the graphene plane and the full LDOS maps are provided in Figure S6.)

As shown in Figure 2e, the bandgap predicted with DFT for both infinite and six-unit-cell GNRs is about 1.6 eV. The more accurate GW approximation was only applied for the infinite GNR, and the band structure in Figure 2e shows a quasi-particle band gap of 3.56 eV, which is consistent with previous studies.^{22,23} It also reveals that the band orders and band shapes within quasi-particle band structures are in agreement with those from Kohn-Sham band structures, confirming the fact that DFT could accurately capture this information for graphene nanostructures;⁴ hence, the LDOS obtained from DFT are reasonable. The simulated LDOS for the six-unit-cell GNR is compared to experimental normalized dI/dV maps in Figure 2g. Because of the huge computational cost, the silicon substrate was not included for the six-unit-cell GNR. (Figures S7 and S8 show additional LDOS maps including the substrate for an infinite GNR.)

The simulated GNR VB-1 and VB states show good agreement with the normalized dI/dV maps. The valence band state at -1.17 V is located at the ends of the GNR, while the VB-1 state observed at -1.43 V is in the middle of the GNR. Analogous finite length effects were previously observed in dI/dV maps of carbon nanowires and straight armchair nanoribbons on gold.^{30,31} The simulated conduction band states also show good agreement with the experimental data, although the observed states appear in a different order. The CB state is predicted to have a density of states concentrated along the edges of the GNR as is observed at $+2.27$ V, and the CB+1 state is predicted to be concentrated at the ends of the GNR. However, a state concentrated at the GNR end is experimentally seen at $+2.0$ V. Since the state at $+2.0$ V appears first, it is assigned as the GNR CB and the state at $+2.27$ V is the GNR CB+1 state. The alignment between the substrate lattice and the GNR may cause energetic shifts in the states as previously observed for carbon nanotubes on InAs.³²

The increased charge density at the GNR edges agrees with previous STM studies of straight atomically precise graphene nanoribbons and GNR heterojunctions on Au(111) where an increased LDOS at the edges was measured.^{2,14,7,33} The enhanced LDOS is not due to an edge state but is instead an extended state with a three-dimensional shape that has a relatively higher value of LDOS with increased height at the outer edges of the GNR.⁷ Localized edge states are seen for 4 nm wide GNRs with disordered edges,³⁴ unzipped carbon nanotubes,³⁵ and zigzag GNRs.⁴ An enhanced DOS is also seen at armchair edges of graphene sheets due to the interference of backscattering electrons.³⁶

The bandgap is determined to be 2.80 eV by choosing the span between the CB and VB onsets, as was done for the STS measurement of chevron GNRs on Au(111).²⁷ Chevron GNRs on Au(111) were shown to have a bandgap of about 2.0 eV,^{6,27} with STS, 2.8 ± 0.03 eV with HREELS,²⁸ and 3.1 ± 0.4 eV with ARUPS.²⁸ Here we provide an experimental measurement of chevron GNRs on H:Si(100) and find a 2.8 eV bandgap. The 2.8 eV bandgap measured here approaches the expected 3.6 eV intrinsic GNR bandgap predicted using the GW approximation.²³ Theoretical modeling has previously shown that the bandgap of a graphene nanoribbon on silicon is expected to be larger than the bandgap of a graphene nanoribbon on gold due to a decreased screening interaction.³⁷ To confirm the reproducibility of the bandgap measurement, line spectra collected over 21 graphene nanoribbons are examined. The

average bandgap is 2.85 eV with a standard deviation of 0.13 eV (Figure S9).

During dry contact transfer overlapping nanoribbons are also placed on the surface allowing the study of multilayer GNRs, which have not been previously examined. While the multilayer GNR cross-junctions that were investigated in this work accidentally formed on a surface during the transfer process, the demonstrated possibility of moving GNRs on H:Si(100) with an STM tip (Figure S4) suggests that such and other complex GNR structures may also be formed intentionally via STM nanomanipulation. Graphene nanoribbon junctions are expected to play an important role in creating novel electronic devices, as has been predicted for in-plane graphene nanowiggle junctions.³⁸ Figure 3a shows several nanoribbons on the

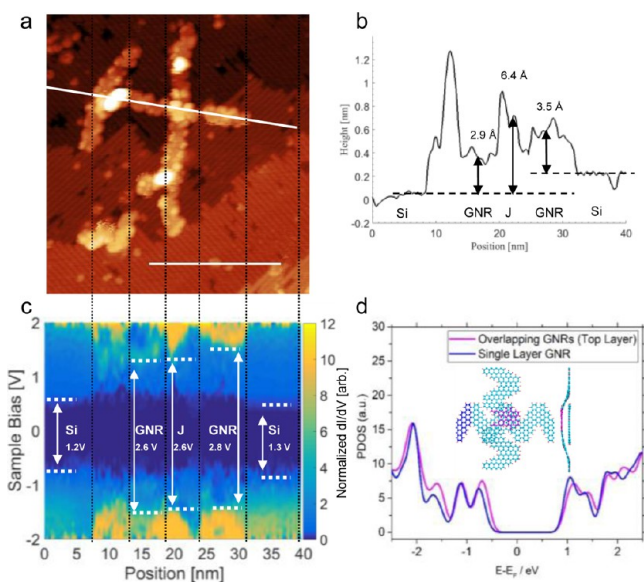


Figure 3. Scanning tunneling spectroscopy (STS) of nanoribbon junctions. (a) STM topograph showing several overlapping graphene nanoribbons. Sample bias: -2 V; tunneling current: 10 pA. Scale bar length is 20 nm. (b) Height profile along solid line in (a). The height of the GNR relative to the surrounding H:Si(100) is 2.9–3.5 Å. The junction appears to be 3–3.5 Å taller than the single layer GNRs. (c) Spectra map taken along the solid line indicated in (a). The regions are labeled Si-H:Si(100) substrate; GNR = graphene nanoribbon, J = the graphene nanoribbon junction. (d) DFT-calculated PDOS for overlapping GNR (top layer) and single-layer GNR, whose atomic structure is shown in the inset. The atoms in the single layer part are colored blue while those in the overlapping region are colored pink.

H:Si(100) surface. Two GNRs greater than 20 nm in length are about 15 nm apart, with a third GNR spanning them to form a junction, labeled J. To the right of the junction, there is a short single layer GNR segment that may have torn off during the DCT process.

Figure 3b shows the height profile along the solid line in Figure 3a. The single layer GNR in the center of the image is 2.9 Å taller than the silicon terrace it sits on, and the short single layer segment on the right is about 3.5 Å taller than the nearby silicon. The junction (J) has an apparent height of 6.4 Å, which is 3.5 Å taller than the GNR beneath it, which is consistent with the expected apparent height of a two-layer GNR junction.

Figure 3c shows a normalized spectra map calculated numerically from the I - V spectroscopy data. The bandgap at

the junction is 2.6 eV. The bandgap over the GNR is estimated as 2.6 eV for the GNR on the left terrace and 2.8 eV for the GNR on the right terrace. The valence band for both single layer GNRs examined is at -1.4 eV; however, the conduction band shifts to a position 0.2 eV lower on the left terrace. Multilayer armchair GNRs are expected to have decreasing bandgaps with increasing layer number.³⁹ Figure 3d shows the PDOS for a two-layer GNR junction calculated by DFT. The overlapping segment has a bandgap slightly smaller than the sections of single layer GNR. The experimental measurement does not show a significant bandgap shift, which is expected given that computational modeling predicts a small bandgap shift.

Previous work on graphene nanoflakes revealed that hydrogen depassivation of a supporting H:Si(100) substrate causes graphene to take on a metallic character due to charge transfer and Si–C bond formation.⁴⁰

Figure 4a shows an STM topograph of a GNR on passivated silicon before hydrogen depassivation. Silicon underneath part of the nanoribbon was depassivated by holding the sample bias at 8 V while moving the tip along the path indicated by the white arrow in Figure 4b at 100 Å/s and maintaining a tunneling current of 0.1 nA. The increased height of the depassivated silicon indicates hydrogen removal and the presence of silicon dangling bonds. (The local density of states of the silicon dangling bonds protrudes farther away the surface than the local density of states corresponding to the hydrogen terminated surface.⁴¹) The apparent height and width of the nanoribbon are reduced after nanolithography as seen in Figure 4b and the height profile in Figure 4f. The 1.5 Å height decrease of the GNR after depassivation indicates an increased coupling to the Si(100) surface. The width decrease reflects a change in the electronic structure of the nanoribbon.

Spectra were collected along the white dashed lines indicated in Figures 4a and 4c. As shown in the normalized dI/dV maps presented in Figures 4d and 4e, the GNR bandgap is 2.9 eV before depassivation. The metallic behavior seen after depassivation is attributed to Si–C bonding that modifies the GNR electronic structure.⁴⁰ While individual Si(100) dangling bonds are metallic, multiple neighboring dangling bonds are semiconducting, indicating that the GNR and not the Si(100) causes the observed metallic behavior.⁴² To explain the electronic changes of the GNR on Si(100) after hydrogen depassivation, we performed DFT simulations to examine the geometry and charge distribution of a GNR on a Si(100) surface before and after hydrogen depassivation. We also show the PDOS of the GNR in Figure 4g. After hydrogen depassivation, the PDOS of the GNR shows finite states at the Fermi level, and there is no longer a bandgap. The dangling bonds at the silicon surface interact with the p_z orbitals of the GNR to form covalent bonds modifying the electronic structure of the GNR and leading to metallic behavior. Figures 4h and 4i show the geometry and normalized charge distribution of the GNR on H:Si(100) and Si(100). Before hydrogen depassivation the GNR is flat above the substrate, and there is no charge density overlap between graphene and H:Si(100). However, after hydrogen depassivation, we see both the geometry and charge distribution change. The surface Si atoms move outward while the GNR above is distorted, and some of the C atoms move inward to the Si surface. The corresponding charge density is strongly localized, and there is some overlap between the GNR and silicon charge densities.

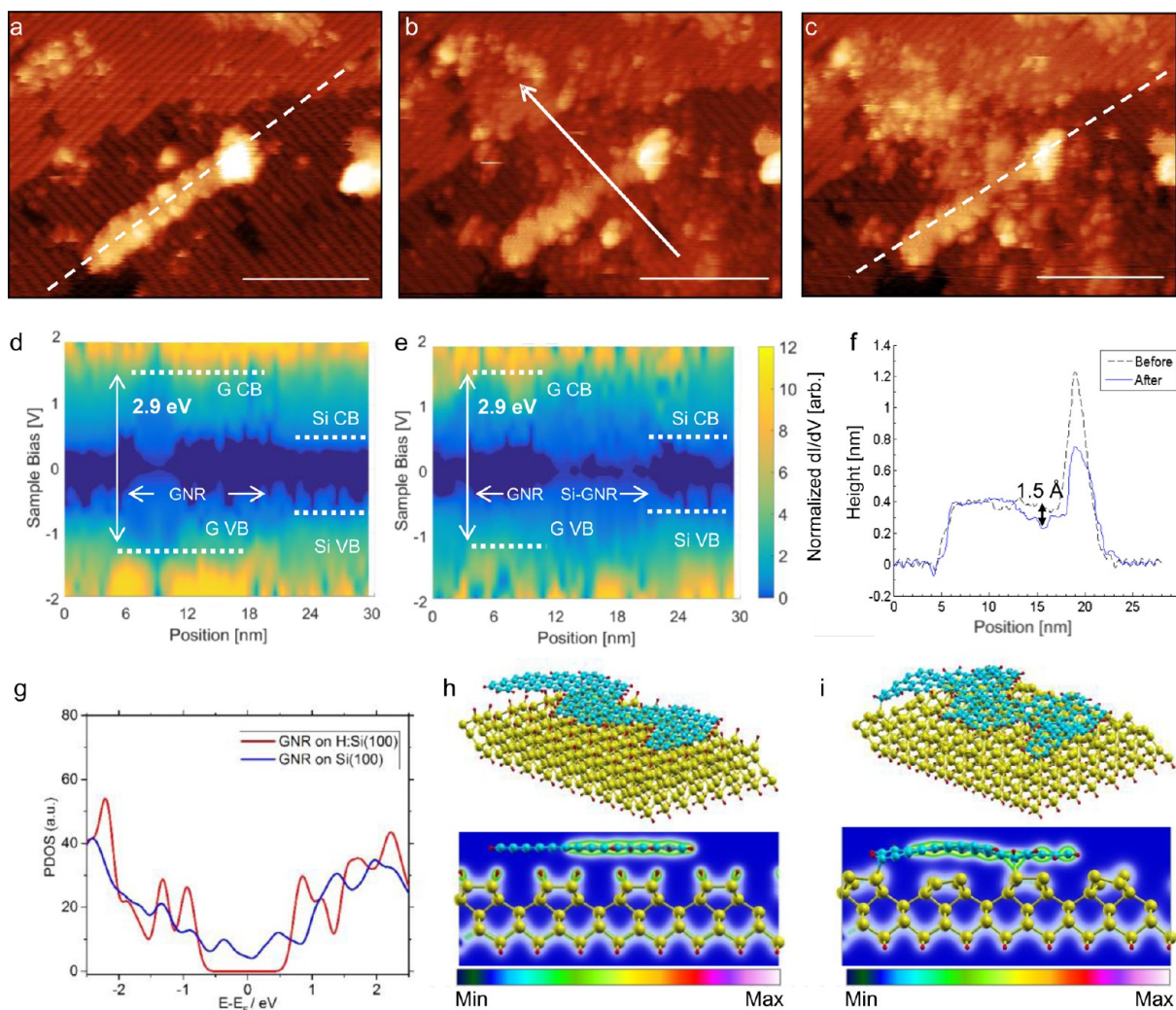


Figure 4. Hydrogen depassivation underneath graphene. (a) STM image of a GNR on H:Si(100). (b) Nanoribbon after hydrogen depassivation lithography. The tip was moved along indicated arrow with a sample bias of +8 V, tunneling current 0.1 nA, and a tip speed of 100 Å/s. The depassivated region appears taller than the surrounding H:Si(100) due to the increased spatial extent of the Si dangling bonds. (c) STM image collected along with STS over the dashed line. Images collected at -2 V 10 pA. All scale bars are 10 nm (d, e) Normalized dI/dV maps corresponding to the spectroscopy collected in (a, c). (f) Height profiles along dashed lines in (a) and (c) to show height changes along GNR after depassivation. (g) Simulated PDOS for GNR on H:Si(100) and Si(100). (h, i) Atomic structures and normalized charge density contour plots for GNR on H:Si(100) and Si(100) shown to visualize the interactions between GNR and the substrate. The cyan, red, and yellow atoms are for C, H, and Si, respectively.

Discussion. Dry contact transfer enables high-resolution STM imaging and spectroscopy of solution-synthesized atomically precise chevron nanoribbons on technologically relevant substrates such as the H:Si(100) 2×1 surface. This method overcomes challenges associated with solvent residue and is very promising for studies of other atomically precise solution-synthesized nanomaterials. The nanoribbons are thin enough that tunneling to the substrate plays a significant role in STS measurements and must be carefully considered to determine the bandgap of GNRs. Through the use of normalized dI/dV images and LDOS simulations, the bandgap of chevron GNRs on H:Si(100) is determined to be 2.85 eV. The ability to cleanly place atomically precise GNRs onto H:Si(100) is unprecedented and is expected to have an enormous impact on GNR device prototyping.

Methods. *Synthesis of GNRs.* Atomically precise chevron GNRs were made in solution by Yamamoto coupling of presynthesized 6,11-dibromo-1,2,3,4-tetraphenyltriphenylene

($C_{42}Br_2H_{26}$) followed by oxidative cyclo-dehydrogenation of the resulting polymer via the Scholl reaction. The synthesis results in a black solid that is filtered and washed to obtain a graphene nanoribbon powder. The synthetic details and materials characterization of solution-synthesized chevron GNRs can be found in our previous works.^{15,16}

Substrate Preparation and STM Experiments. STM imaging was performed with a home-built Lyding style STM⁴³ operating under ultrahigh vacuum (base pressure 3×10^{-11} Torr). Imaging is performed under constant current mode at room temperature (sample bias -2 V, tunneling current 10 pA). H:Si(100) is prepared by degassing a Si(100) substrate at 600 °C for 8–16 h, flashing at 1200 °C for 5–30 s several times, and holding the sample at 377 °C during exposure to 1200 langmuirs of atomic hydrogen. The silicon wafers used are Sb-doped Montco n-Si(100) (sheet resistance 5–20 m Ω ·cm) and B-doped Montco p-Si(100) (sheet resistance 0.01–0.02 Ω ·cm). Iridium-coated field-directed

sputter sharpened tungsten probes from TipTek, and etched platinum–iridium tips were used for STS and STM imaging experiments. Images were also collected with etched tungsten probes. The DCT applicator is prepared by fraying a piece of fiberglass and coating it with GNR powder. The applicator is transferred into UHV and degassed at elevated temperatures overnight. Nanoribbons are exfoliated onto the silicon surface by pressing the fiberglass applicator against the sample. Scanning tunneling spectroscopy (STS) is collected in variable spacing mode ($dS = 2 \text{ \AA}$), with an initial set-point tunneling current of 100 pA. To convert to constant spacing STS data, the raw data are scaled by an exponential factor to account for the change in current due to change in tip–sample separation.⁴⁴ Hydrogen depassivation lithography is performed by moving the tip at 100 $\text{\AA}/s$ while maintaining a sample bias of 8 V and a tunneling current of 0.1 nA.

Computational Modeling. Density functional theory calculations for a six-unit-cell GNR were performed with Quantum Espresso package,⁴⁵ with a supercell arranged to separate GNR and its images. Norm-conserving pseudopotentials with the Perdew–Burke–Ernzerhof (PBE) exchange–correlation functional⁴⁶ were employed, with a plane-wave energy cutoff of 100 Ry. A Monkhorst–Pack grid of $1 \times 1 \times 1$ was used for structural relaxations and $2 \times 2 \times 1$ for electronic property calculations. The structures were relaxed until the maximum residual force was smaller than 0.05 eV/\AA . For the systems of GNR on hydrogen passivated and depassivated silicon surface, due to the lattice mismatch, a GNR supercell of two unit cells was placed upon the substrate with five layers of silicon atoms. Tensile and compressive strain were applied to the GNR and silicon substrate, respectively, whose magnitudes were all less than 1% to ensure the electronic properties of the systems were not altered too much. The Grimme-D2 van der Waals corrections⁴⁷ were used to describe the interaction between the GNR and the substrate. The structures were also relaxed with a Monkhorst–Pack grid of $1 \times 1 \times 1$ until the maximum residual force was smaller than 0.05 eV/\AA . Then the PDOS and charge distribution were calculated with a Monkhorst–Pack grid of $2 \times 1 \times 1$. The visualization of geometries and LDOS was performed with XCrysDen.⁴⁸

The DFT and GW band structures for an infinite GNR with periodic boundary condition were calculated using the VASP package^{49,50} within the Perdew–Burke–Ernzerhof (PBE) exchange–correlation functional.⁴⁶ The projector augmented wave (PAW) pseudopotentials with a 400 eV energy cutoff were used. The Gamma-point-centered k -point of $4 \times 1 \times 1$ was applied for structural relaxation and band structure calculations. The structure was relaxed until the maximum residual force was less than 0.01 eV/\AA . Starting from DFT ground state, quasi-particle energies were calculated using the single-shot G0W0 approximation⁵¹ implemented in VASP. Concerning the memory requirement and computational time, the key parameters of NBANDS = 512, ENCUT = 400, ENCUTGW = 80, and NOMEGA = 36 were used to conduct the GW simulation. These parameter settings were similar to those listed in a previous study.⁵²

■ ASSOCIATED CONTENT

📄 Supporting Information

The Supporting Information is available free of charge on the ACS Publications website at DOI: 10.1021/acs.nanolett.6b03709.

Additional analysis of chevron GNRs on H:Si(100) including height distributions, manipulation of GNRs with the STM probe, DFT modeling results, and scanning tunneling spectroscopy data (PDF)

■ AUTHOR INFORMATION

Corresponding Author

*E-mail: lyding@illinois.edu (J.L.).

ORCID

Alexander Sinitskii: 0000-0002-8688-3451

Joseph W. Lyding: 0000-0001-7285-4310

Author Contributions

T.H.V. and A.S. synthesized the GNRs, A.R. and J.W.L. performed the STM experiments, and T.S. and N.R.A. performed the simulations. All authors discussed the results and contributed to writing the manuscript.

Funding

The work on the synthesis of GNRs was supported by the National Science Foundation (NSF) through CHE-1455330 and by the Office of Naval Research (ONR) through N00014-16-1-2899. The materials characterization of GNRs was performed in part in Central Facilities of the Nebraska Center for Materials and Nanoscience (NCMN), which is supported by the Nebraska Research Initiative. The STM work by A.R. and J.W.L. was supported by the Office of Naval Research under grant # N00014-13-1-0300. T.S. and N.R.A. are supported by AFOSR under grant # FA9550-12-1-0464 and by NSF under grants 1264282, 1420882, 1506619, and 1545907.

Notes

The authors declare no competing financial interest.

■ ACKNOWLEDGMENTS

All the simulations were performed on the Blue Water computation resources provided by the University of Illinois. The authors thank Dr. Liangbo Liang for his kind help with GW calculations.

■ ABBREVIATIONS

GNR, graphene nanoribbon; STM, scanning tunneling microscopy; STS, scanning tunneling spectroscopy; CITS, current imaging tunneling spectroscopy; DCT, dry contact transfer; LDOS, local density of states; DFT, density functional theory.

■ REFERENCES

- (1) Cai, J.; Ruffieux, P.; Jaafar, R.; Bieri, M.; Braun, T.; Blankenburg, S.; Muoth, M.; Seitsonen, A. P.; Saleh, M.; Feng, X.; Mullen, K.; Fasel, R. Atomically precise bottom-up fabrication of graphene nanoribbons. *Nature* **2010**, *466* (7305), 470–3.
- (2) Chen, Y. C.; de Oteyza, D. G.; Pedramrazi, Z.; Chen, C.; Fischer, F. R.; Crommie, M. F. Tuning the band gap of graphene nanoribbons synthesized from molecular precursors. *ACS Nano* **2013**, *7* (7), 6123–6128.
- (3) Abdurakhmanova, N.; Amsharov, N.; Stepanow, S.; Jansen, M.; Kern, K.; Amsharov, K. Synthesis of wide atomically precise graphene nanoribbons from para-oligophenylene based molecular precursor. *Carbon* **2014**, *77*, 1187–1190.
- (4) Ruffieux, P.; Wang, S.; Yang, B.; Sánchez-Sánchez, C.; Liu, J.; Diemel, T.; Talirz, L.; Shinde, P.; Pignedoli, C. A.; Passerone, D.; Dumslaff, T.; Feng, X.; Müllen, K.; Fasel, R. On-surface synthesis of graphene nanoribbons with zigzag edge topology. *Nature* **2016**, *531* (7595), 489–492.

- (5) Bronner, C.; Haase, A.; Tegeder, P. Image potential states at chevron-shaped graphene nanoribbons /Au(111) interfaces. *Phys. Rev. B: Condens. Matter Mater. Phys.* **2015**, *91* (4), 4422–4425.
- (6) Cai, J.; Pignedoli, C. A.; Talirz, L.; Ruffieux, P.; Söde, H.; Liang, L.; Meunier, V.; Berger, R.; Li, R.; Feng, X. Graphene nanoribbon heterojunctions. *Nat. Nanotechnol.* **2014**, *9* (11), 896–900.
- (7) Chen, Y. C.; Cao, T.; Chen, C.; Pedramrazi, Z.; Haberger, D.; de Oteyza, D. G.; Fischer, F. R.; Louie, S. G.; Crommie, M. F. Molecular bandgap engineering of bottom-up synthesized graphene nanoribbon heterojunctions. *Nat. Nanotechnol.* **2015**, *10* (2), 156–60.
- (8) Bronner, C.; Stremmlau, S.; Gille, M.; Brausse, F.; Haase, A.; Hecht, S.; Tegeder, P. Aligning the band gap of graphene nanoribbons by monomer doping. *Angew. Chem., Int. Ed.* **2013**, *52* (16), 4422–4425.
- (9) Vo, T. H.; Shekhirev, M.; Kunkel, D. A.; Orange, F.; Guinel, M. J.; Enders, A.; Sinitskii, A. Bottom-up solution synthesis of narrow nitrogen-doped graphene nanoribbons. *Chem. Commun. (Cambridge, U. K.)* **2014**, *50* (32), 4172–4.
- (10) Kawai, S.; Saito, S.; Osumi, S.; Yamaguchi, S.; Foster, A. S.; Spijker, P.; Meyer, E. Atomically controlled substitutional boron-doping of graphene nanoribbons. *Nat. Commun.* **2015**, *6*, 8098.
- (11) Chen, C.-C.; Chang, Y.-C. Theoretical studies of graphene nanoribbon quantum dot qubits. *Phys. Rev. B: Condens. Matter Mater. Phys.* **2015**, *92* (24), 245406.
- (12) Trauzettel, B.; Bulaev, D. V.; Loss, D.; Burkard, G. Spin qubits in graphene quantum dots. *Nat. Phys.* **2007**, *3* (3), 192–196.
- (13) Bennett, P. B.; Pedramrazi, Z.; Madani, A.; Chen, Y.-C.; de Oteyza, D. G.; Chen, C.; Fischer, F. R.; Crommie, M. F.; Bokor, J. Bottom-up graphene nanoribbon field-effect transistors. *Appl. Phys. Lett.* **2013**, *103* (25), 253114.
- (14) Jacobberger, R. M.; Kiraly, B.; Fortin-Deschenes, M.; Levesque, P. L.; McElhinny, K. M.; Brady, G. J.; Rojas Delgado, R.; Singha Roy, S.; Mannix, A.; Lagally, M. G.; Evans, P. G.; Desjardins, P.; Martel, R.; Hersam, M. C.; Guisinger, N. P.; Arnold, M. S. Direct oriented growth of armchair graphene nanoribbons on germanium. *Nat. Commun.* **2015**, *6*, 8006.
- (15) Vo, T. H.; Shekhirev, M.; Kunkel, D. A.; Morton, M. D.; Berglund, E.; Kong, L.; Wilson, P. M.; Dowben, P. A.; Enders, A.; Sinitskii, A. Large-scale solution synthesis of narrow graphene nanoribbons. *Nat. Commun.* **2014**, *5*, 3189.
- (16) Vo, T. H.; Shekhirev, M.; Lipatov, A.; Korlacki, R. A.; Sinitskii, A. Bulk properties of solution-synthesized chevron-like graphene nanoribbons. *Faraday Discuss.* **2014**, *173*, 105–13.
- (17) Schwab, M. G.; Narita, A.; Hernandez, Y.; Balandina, T.; Mali, K. S.; De Feyter, S.; Feng, X.; Mullen, K. Structurally defined graphene nanoribbons with high lateral extension. *J. Am. Chem. Soc.* **2012**, *134* (44), 18169–72.
- (18) Narita, A.; Feng, X.; Hernandez, Y.; Jensen, S. A.; Bonn, M.; Yang, H.; Verzhbitskiy, I. A.; Casiraghi, C.; Hansen, M. R.; Koch, A. H.; Fytas, G.; Ivasenko, O.; Li, B.; Mali, K. S.; Balandina, T.; Mahesh, S.; De Feyter, S.; Mullen, K. Synthesis of structurally well-defined and liquid-phase-processable graphene nanoribbons. *Nat. Chem.* **2013**, *6* (2), 126–132.
- (19) Albrecht, P. M.; Lyding, J. W. Ultrahigh-vacuum scanning tunneling microscopy and spectroscopy of single-walled carbon nanotubes on hydrogen-passivated Si(100) surfaces. *Appl. Phys. Lett.* **2003**, *83* (24), 5029–5031.
- (20) Ritter, K. A.; Lyding, J. W. The influence of edge structure on the electronic properties of graphene quantum dots and nanoribbons. *Nat. Mater.* **2009**, *8* (3), 235–42.
- (21) He, K. T.; Koepke, J. C.; Barraza-Lopez, S.; Lyding, J. W. Separation-Dependent Electronic Transparency of Monolayer Graphene Membranes on III–V Semiconductor Substrates. *Nano Lett.* **2010**, *10* (9), 3446–3452.
- (22) Wang, S.; Wang, J. Quasiparticle Energies and Optical Excitations in Chevron-Type Graphene Nanoribbon. *J. Phys. Chem. C* **2012**, *116* (18), 10193–10197.
- (23) Liang, L.; Meunier, V. Electronic structure of assembled graphene nanoribbons: Substrate and many-body effects. *Phys. Rev. B: Condens. Matter Mater. Phys.* **2012**, *86* (19), 195404.
- (24) Neaton, J. B.; Hybertsen, M. S.; Louie, S. G. Renormalization of Molecular Electronic Levels at Metal-Molecule Interfaces. *Phys. Rev. Lett.* **2006**, *97* (21), 216405.
- (25) Thygesen, K. S.; Rubio, A. Renormalization of Molecular Quasiparticle Levels at Metal-Molecule Interfaces: Trends across Binding Regimes. *Phys. Rev. Lett.* **2009**, *102* (4), 216405.
- (26) Talirz, L.; Ruffieux, P.; Fasel, R. On-Surface Synthesis of Atomically Precise Graphene Nanoribbons. *Adv. Mater.* **2016**, *28* (29), 6222–6231.
- (27) Vo, T. H.; Perera, U. G.; Shekhirev, M.; Mehdi Pour, M.; Kunkel, D. A.; Lu, H.; Gruverman, A.; Sutter, E.; Cotlet, M.; Nykypanchuk, D.; Zahl, P.; Enders, A.; Sinitskii, A.; Sutter, P. Nitrogen-Doping Induced Self-Assembly of Graphene Nanoribbon-Based Two-Dimensional and Three-Dimensional Metamaterials. *Nano Lett.* **2015**, *15* (9), 5770–7.
- (28) Linden, S.; Zhong, D.; Timmer, A.; Aghdassi, N.; Franke, J. H.; Zhang, H.; Feng, X.; Müllen, K.; Fuchs, H.; Chi, L.; Zacharias, H. Electronic Structure of Spatially Aligned Graphene Nanoribbons on Au(788). *Phys. Rev. Lett.* **2012**, *108* (21), 216801.
- (29) Ruffieux, P.; Cai, J.; Plumb, N. C.; Patthey, L.; Prezzi, D.; Ferretti, A.; Molinari, E.; Feng, X.; Mullen, K.; Pignedoli, C. A.; Fasel, R. Electronic structure of atomically precise graphene nanoribbons. *ACS Nano* **2012**, *6* (8), 6930–5.
- (30) Kimouche, A.; Ervasti, M. M.; Drost, R.; Halonen, S.; Harju, A.; Joensuu, P. M.; Sainio, J.; Liljeroth, P. Ultra-narrow metallic armchair graphene nanoribbons. *Nat. Commun.* **2015**, *6*, 10177.
- (31) Vasseur, G.; Fagot-Revurat, Y.; Sicot, M.; Kierren, B.; Moreau, L.; Malterre, D.; Cardenas, L.; Galeotti, G.; Lipton-Duffin, J.; Rosei, F.; Di Giovannantonio, M.; Contini, G.; Le Fevre, P.; Bertran, F.; Liang, L.; Meunier, V.; Perepichka, D. F. Quasi one-dimensional band dispersion and surface metallization in long-range ordered polymeric wires. *Nat. Commun.* **2016**, *7*, 10235.
- (32) Ruppalt, L. B.; Lyding, J. W. Charge transfer between semiconducting carbon nanotubes and their doped GaAs(110) and InAs(110) substrates detected by scanning tunnelling spectroscopy. *Nanotechnology* **2007**, *18* (21), 215202.
- (33) Söde, H.; Talirz, L.; Gröning, O.; Pignedoli, C. A.; Berger, R.; Feng, X.; Müllen, K.; Fasel, R.; Ruffieux, P. Electronic band dispersion of graphene nanoribbons via Fourier-transformed scanning tunneling spectroscopy. *Phys. Rev. B: Condens. Matter Mater. Phys.* **2015**, *91* (4), 045429.
- (34) Pan, M.; Girao, E. C.; Jia, X.; Bhaviripudi, S.; Li, Q.; Kong, J.; Meunier, V.; Dresselhaus, M. S. Topographic and spectroscopic characterization of electronic edge states in CVD grown graphene nanoribbons. *Nano Lett.* **2012**, *12* (4), 1928–33.
- (35) Tao, C.; Jiao, L.; Yazyev, O. V.; Chen, Y.-C.; Feng, J.; Zhang, X.; Capaz, R. B.; Tour, J. M.; Zettl, A.; Louie, S. G.; Dai, H.; Crommie, M. F. Spatially resolving edge states of chiral graphene nanoribbons. *Nat. Phys.* **2011**, *7* (8), 616–620.
- (36) Park, C.; Yang, H.; Mayne, A. J.; Dujardin, G.; Seo, S.; Kuk, Y.; Ihm, J.; Kim, G. Formation of unconventional standing waves at graphene edges by valley mixing and pseudospin rotation. *Proc. Natl. Acad. Sci. U. S. A.* **2011**, *108* (46), 18622–5.
- (37) Kharache, N.; Meunier, V. Width and Crystal Orientation Dependent Band Gap Renormalization in Substrate-Supported Graphene Nanoribbons. *J. Phys. Chem. Lett.* **2016**, *7* (8), 1526–33.
- (38) Cary, T.; Girão, E. C.; Meunier, V. Electronic properties of three-terminal graphitic nanowiggles. *Phys. Rev. B: Condens. Matter Mater. Phys.* **2014**, *90* (11), 115409.
- (39) Kharache, N.; Zhou, Y.; O'Brien, K. P.; Kar, S.; Nayak, S. K. Effect of Layer Stacking on the Electronic Structure of Graphene Nanoribbons. *ACS Nano* **2011**, *5* (8), 6096–6101.
- (40) Xu, Y.; He, K. T.; Schmucker, S. W.; Guo, Z.; Koepke, J. C.; Wood, J. D.; Lyding, J. W.; Aluru, N. R. Inducing electronic changes in graphene through silicon (100) substrate modification. *Nano Lett.* **2011**, *11* (7), 2735–42.

(41) Lyding, J.; Shen, T. C.; Hubacek, J.; Tucker, J.; Abeln, G. Nanoscale patterning and oxidation of H-passivated Si (100)-2×1 surfaces with an ultrahigh vacuum scanning tunneling microscope. *Appl. Phys. Lett.* **1994**, *64* (15), 2010–2012.

(42) Ye, W.; Min, K.; Peña Martin, P.; Rockett, A. A.; Aluru, N. R.; Lyding, J. W. Scanning tunneling spectroscopy and density functional calculation of silicon dangling bonds on the Si(100)-2 × 1:H surface. *Surf. Sci.* **2013**, *609*, 147–151.

(43) Lyding, J.; Skala, S.; Hubacek, J.; Brockenbrough, R.; Gammie, G. Variable-Temperature Scanning Tunneling Microscope. *Rev. Sci. Instrum.* **1988**, *59* (9), 1897–1902.

(44) Ruppalt, L. B.; Lyding, J. W. Metal-Induced Gap States at a Carbon-Nanotube Intramolecular Heterojunction Observed by Scanning Tunneling Microscopy. *Small* **2007**, *3* (2), 280–284.

(45) Giannozzi, P.; Baroni, S.; Bonini, N.; Calandra, M.; Car, R.; Cavazzoni, C.; Ceresoli, D.; Chiarotti, G. L.; Cococcioni, M.; Dabo, I.; Dal Corso, A.; de Gironcoli, S.; Fabris, S.; Fratesi, G.; Gebauer, R.; Gerstmann, U.; Gougoussis, C.; Kokalj, A.; Lazzeri, M.; Martin-Samos, L.; Marzari, N.; Mauri, F.; Mazzarello, R.; Paolini, S.; Pasquarello, A.; Paulatto, L.; Sbraccia, C.; Scandolo, S.; Sclauzero, G.; Seitsonen, A. P.; Smogunov, A.; Umari, P.; Wentzcovitch, R. M. QUANTUM ESPRESSO: a modular and open-source software project for quantum simulations of materials. *J. Phys.: Condens. Matter* **2009**, *21* (39), 395502.

(46) Perdew, J. P.; Burke, K.; Ernzerhof, M. Generalized gradient approximation made simple. *Phys. Rev. Lett.* **1996**, *77* (18), 3865.

(47) Grimme, S. Semiempirical GGA-type density functional constructed with a long-range dispersion correction. *J. Comput. Chem.* **2006**, *27* (15), 1787–1799.

(48) Kokalj, A. XCrySDen—a new program for displaying crystalline structures and electron densities. *J. Mol. Graphics Modell.* **1999**, *17* (3–4), 176–179.

(49) Kresse, G.; Furthmüller, J. Efficiency of ab-initio total energy calculations for metals and semiconductors using a plane-wave basis set. *Comput. Mater. Sci.* **1996**, *6* (1), 15–50.

(50) Kresse, G.; Furthmüller, J. Efficient iterative schemes for ab initio total-energy calculations using a plane-wave basis set. *Phys. Rev. B: Condens. Matter Mater. Phys.* **1996**, *54* (16), 11169.

(51) Shishkin, M.; Kresse, G. Self-consistent G W calculations for semiconductors and insulators. *Phys. Rev. B: Condens. Matter Mater. Phys.* **2007**, *75* (23), 235102.

(52) Liang, L.; Meunier, V. Atomically Precise Graphene Nanoribbon Heterojunctions for Excitonic Solar Cells. *J. Phys. Chem. C* **2014**, *119* (1), 775–783.